Engineering Structures 344 (2025) 121316

Contents lists available at ScienceDirect

Engineering Structures

journal homepage: www.elsevier.com/locate/engstruct

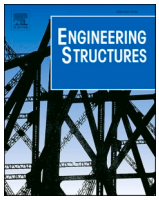

On the influence of the relative humidity on the thermal response of a concrete plate: A mesoscale phase-field analysis

Hui Wang [a,*], Luyao Liu [a], Xi Chen [b], Wei Jiang [c], Herbert A. Mang [d,e], Bernhard Pichler [d,*]

[a] School of Ocean and Civil Engineering, Shanghai Jiao Tong University, Shanghai, China
[b] College of Civil Engineering and Architecture, Jiaxing University, Jiaxing, China
[c] School of Materials Science and Engineering, Tongji University, Shanghai, China
[d] Institute for Mechanics of Materials and Structures, TU Wien, Karlsplatz 13/202, Vienna 1040, Austria
[e] College of Civil Engineering, Tongji University, Shanghai, China

ARTICLE INFO

Keywords:
Thermal responses
Mesoscale
Phase-field
Relative humidity
Cracking

ABSTRACT

This study contains an investigation of the thermomechanical response and the cracking behavior of a concrete plate, subjected to diurnal temperature changes, with a particular focus on the influence of the relative humidity (*RH*). The latter contributes to the heterogeneity of the thermal expansion of the concrete constituents and, thereby, has an influence on the mesoscopic cracking behavior. In the present work, a mesoscale thermo-mechanical phase-field fracture model is established, considering the mesostructure of concrete, consisting of mortar, aggregates, and interfacial transition zones (ITZs). The ITZs are regularized with an auxiliary interfacial phase-field. The mesoscale results are compared with the ones from macroscopic phase-field analyses. It is found that, while the relative humidity exhibits an insignificant impact on the macrostresses, it has a significant influence on the mesostress fluctuations and the fracture damage. Astonishingly, mesocracking even occurs in macroscopically-compressed regions of the plate. This is primarily due to the large *RH*-dependent expansive thermal eigenstrains in the mortar, which result in tensile stresses in the aggregates and the ITZs, and in an increase of risk of mesocracking. These cracks start in the ITZs. Their propagation and orientation are governed by the local principal stresses. This agrees with the results of microelastic analyses. Therefore, both the mesoscale phase-field simulations and the microelastic models can be employed to predict the initiation of cracking, providing insight into the design and the durability assessment of thermally-loaded concrete structures.

1. Introduction

Concrete structures are generally subjected to cyclic changes in ambient temperature and humidity [1–3]. Restrained thermal eigenstrains, as products of the temperature change and the thermal expansion coefficient [4], result in thermal stresses and cracking [5–7]. This can entail degradation of the elastic stiffness and strength of concrete materials [8–10] and, furthermore, loss of durability of concrete structures [11,12].

The thermal expansion coefficient of concrete is critical for the quantification of thermal stresses. It depends on the initial composition, the maturity, and the internal relative humidity [4,13–15]. The type of aggregates, occupying a substantial volume fraction of around 70 % for typical concretes [16,17], apparently determines the magnitude of its thermal expansion coefficient. For example, concrete containing siliceous aggregates generally exhibits a larger thermal expansion coefficient, compared to concrete containing carbonate aggregates [18,19]. The thermal expansion coefficient of concrete decreases, in most cases, almost linearly with increasing volume fraction of the coarse aggregates [15,20]. This is primarily attributed to the smaller thermal expansion coefficient of commonly used aggregates, compared to that of the cement paste [15]. The latter, in turn, is a bell-shaped function of the internal relative humidity [14,21]. Notably, *RH* can be translated into the water saturation degree of concrete provided that sorption isotherms are known [22]. The thermal expansion coefficient of cement paste peaks at around $RH = 65\%$. At this level of partial saturation, it is almost twice as large as the minimum value which refers to $RH = 100\%$, i.e. to full water saturation, as shown in Fig. 6 in Subsection 3.1. The nontrivial thermal expansion behavior of cement paste is a consequence of the reversible and quasi-instantaneous uptake/release of water by

* Corresponding authors.
E-mail addresses: hui.wang@sjtu.edu.cn (H. Wang), bernhard.pichler@tuwien.ac.at (B. Pichler).

https://doi.org/10.1016/j.engstruct.2025.121316
Received 12 April 2025; Received in revised form 18 August 2025; Accepted 8 September 2025
Available online 23 September 2025

nanoscopic cement hydrates, which is induced by decreasing/increasing the temperature of the material [21,23]. The temperature-change-induced nanoscopic water migration effect results in changes of the curvature of the menisci between water-filled and gas-filled parts of the nanoscopic porosity, and this leads to both (i) measurable changes of the internal relative humidity (referred to as hygrothermic coefficients) and (ii) of the underpressure experienced by the water-filled porosity. The changed pore underpressure, in turn, results in a poromechanical contribution to macroscopic volume changes, and this manifests itself macroscopically as a non-orthodox thermal expansion behavior [21,23]. Because the thermal expansion coefficient of cement paste is a nonlinear function of the internal relative humidity, also the thermal expansion behavior of concrete and the corresponding thermal stresses depend on the saturation state of the material [15]. This provides the motivation for the present work to study the thermal response of a concrete plate by explicitly considering different levels of internal relative humidity, covering partial saturation ($RH = 50\%$ and $RH = 65\%$) and full saturation ($RH = 100\%$).

The influence of the internal relative humidity on the thermal response affects the thermal conductivity [24,25], the thermal deformation [4,26], and the potential degradation related to microcracking. As the moisture content increases, the thermal conductivity of concrete generally increases, consideration of which is essential for accurate determination of the temperature field. The latter, together with the relative humidity-dependent thermal expansion coefficient, provides access to the evolution of the thermal eigenstresses. The corresponding macroscopic thermal stresses vary only slightly with the change of the relative humidity, but the microscopic thermal stress fluctuations between the cement paste and the aggregates depend strongly on the relative humidity [27]. These fluctuations underline the risk of microcracking, particularly in the interfacial transition zones (ITZs) between the aggregates and the surrounding cement paste. To account for this situation, mesoscopic thermoelastic damage modeling and Scanning Electron Microscopy (SEM) were utilized to study the microscopic cracking of concrete, subjected to high temperatures [28,29]. Thermomechanical modeling of concrete has mainly evolved in the continuum and discrete mechanics. Continuum-based approaches include, e.g., cohesive zone models [30,31], peridynamic models [32,33], and the crack band method [34]. They have demonstrated the capability of capturing thermomechanical damage of concrete at the mesoscale. These methods often face the challenge of mesh sensitivity [35,36]. In addition, failure of the ITZs is frequently modeled in an oversimplified manner. Recently, phase-field damage modeling [37,38] has emerged as a promising alternative for thermal fracture analysis. Discrete mechanics approaches include, e.g., the discrete element method [39,40] and lattice models [41]. They explicitly account for the microstructural granular interactions of concrete. However, this comes at high computational costs when simulating multiscale cracking under thermomechanical loading at structural scales. In the present work, the risk of cracking of concrete structures, subjected to moderate ambient thermal loading, is quantified in the framework of a phase-field damage model.

The phase-field model of fracture, established on the basis of the Griffith's theory and the Frankfort-Marigo variational principle, is capable of capturing the initiation, propagation, and intricate networking of cracks [42–44]. The discrete crack surface is regularized to a smeared cracking zone, characterized by an auxiliary scalar variable. This regularization facilitates the smooth transition between cracked and intact regions. Progressive macrocracking can be simulated by solving partial differential equations for multifield problems without pre-defining of the cracking path. The phase-field model was successfully applied e.g. to brittle fracture [44,45], dynamic fracture [42,46], fatigue fracture [47,48], and blasting failure [49]. Because of the heterogeneous microstructure of concrete, consisting of the cement paste matrix, aggregate inclusions, and ITZs, simulation of microcracking is nontrivial, especially when considering the ultrathin nature of the ITZs. Seen from this point of view, an auxiliary phase-field was introduced to regularize the ITZs to smeared zones [50], which can capture both matrix cracking and interfacial debonding in case of, for example, corrosion-induced cracking [51] and FRP-to-concrete bonding failure [52]. In the present work, the mesoscale phase-field model is further extended to address thermomechanical problems for concrete, providing insight into thermally-induced cracking of concrete.

Herein, the dependence of the thermal response of concrete structures on the relative humidity is investigated by means of a mesoscale thermomechanical phase-field model. While the preceding discussion of existing literature highlights the capability of various thermomechanical models, either continuum-based [30–34] or discrete [39–41], a critical research gap remains in the explicit, multiscale connection between internal relative humidity and thermal cracking. In particular, a comprehensive integration of the nonlinear, *RH*-dependent thermal properties of the cementitious matrix [14,21] into a fracture mechanics framework, capable of resolving the complex failure modes of ITZs, represents a critical and largely unmet challenge. The present study addresses this gap by resolving the mesostructure of concrete into a mortar matrix, aggregate inclusions, and ITZs. The discrete crack surfaces are introduced as smeared crack phases. The ultrathin ITZs are regularized with an auxiliary interphasial phase-field. This allows for capturing bulk matrix cracking, interfacial debonding, and their interaction and, thereby, quantifying *RH*-driven mesoscopic stress fluctuations and crack patterns, which is typically overlooked in existing macroscopic analyses [27]. As far as possible, simulation results are validated by an analytical microelastic model, demonstrating the predictive capacity of the proposed model. Overall, the present study provides multiscale insight into thermally-induced cracking of concrete that explicitly couples *RH*-dependent material properties with mesocracking mechanisms.

The remainder of this paper is structured as follows: The elements of the mesoscale thermomechanical phase-field model for concrete are described in Section 2. The established model is then in Section 3 exemplarily applied to a concrete pavement slab, subjected to a diurnal temperature change. Discussions on the mesoscopic stresses and the cracking behavior, as well as sensitivity analyses, are continued in Section 4, followed by concluding remarks drawn in Section 5.

2. Mesoscale thermomechanical phase-field model for concrete

2.1. Thermomechanical phase-field model for brittle fracture

An arbitrary solid material body Ω contains a matrix Ω_m and an inclusion Ω_i, surrounded by the ultrathin interface Γ_{ITZ} in-between. In the framework of a phase-field model for fracture, the discrete crack surface Γ_c in Fig. 1(a) is approximated by a continuous smeared crack, characterized by an auxiliary scalar variable ϕ. The latter varies from 0 to 1, representing the transition from the intact (uncracked) state to a fully-damaged state, see Fig. 1(b). The solid body is subjected to boundary conditions, including the traction $\vec{t}$, the displacement $\vec{u}_\Gamma$, the heat flux $\vec{q}_\Gamma$, and the temperature T_Γ, with $\partial\Omega = \partial\Omega_u \cup \partial\Omega_t$ ($\partial\Omega_u \cap \partial\Omega_t = \varnothing$) and

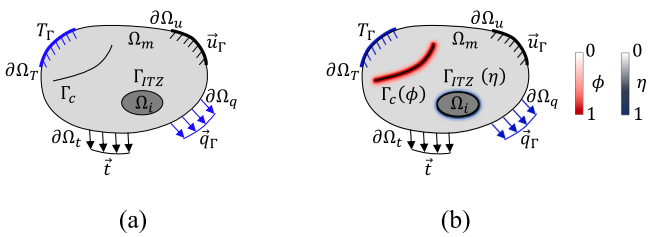

Fig. 1. Schematic representation of a solid material body with (a) a discrete crack Γ_c and ultrathin interface Γ_{ITZ} and (b) a smeared crack $\Gamma_c(\phi)$ and a smeared interphase $\Gamma_{ITZ}(\eta)$.

$\partial\Omega = \partial\Omega_q \cup \partial\Omega_T$ ($\partial\Omega_q \cap \partial\Omega_T = \varnothing$).

The Lagrangian energy functional, $\mathscr{L}$, of the material body is obtained as the sum of the kinetic energy, elastic energy, fracture energy, thermal energy, and of the external energy, i.e.

$$\mathscr{L} = \int_\Omega \left\{ \frac{1}{2}\rho \dot{\vec{u}}\cdot\dot{\vec{u}} - \psi_e(\boldsymbol{\varepsilon_e}, \phi) - G_c\gamma_d(\phi, \nabla\phi) + \left(\rho c_p \dot{T} + \nabla\vec{q} - \Phi\right) + \vec{b}\cdot\vec{u} \right\} dV + \int_{\partial\Omega_t} \vec{t}\cdot\vec{u}\, dS + \int_{\partial\Omega_q} \vec{q}\cdot\vec{n}\, dS, \tag{1}$$

with $\vec{u}$ as the displacement vector and $\dot{\vec{u}} = \frac{\partial \vec{u}}{\partial t}$ as the velocity vector. The material is characterized by a mass density ρ, a specific heat capacity c_p, a body force vector $\vec{b}$, and an internal heat source Φ. The term $\psi_e(\boldsymbol{\varepsilon_e}, \phi)$ stands for the elastic energy density; G_c denotes the critical energy release rate. The crack surface density $\gamma_d(\phi, \nabla\phi)$ is defined as [42]

$$\gamma_d(\phi, \nabla\phi) = \frac{\phi^2}{2l_0} + \frac{l_0}{2}\nabla\phi\cdot\nabla\phi, \tag{2}$$

with l_0 denoting the length-scale parameter (internal length), which characterizes the width of the regularized crack phase. As shown in the following study, $l_0 = 3.8$ mm, satisfies the condition that l_0 has to be at least twice as large as the mesh size, $l_0 \geq 2h_{mesh}$, with $h_{mesh} = 0.7$ mm, and it ensures a sufficiently refined resolution of the phase-field transition zone.

The elastic energy density $\psi_e(\boldsymbol{\varepsilon_e}, \phi)$ depends on the phase-field ϕ and the elastic strain $\boldsymbol{\varepsilon_e}$. The latter is defined as

$$\boldsymbol{\varepsilon_e} = \boldsymbol{\varepsilon} - \boldsymbol{\varepsilon}_T^e, \tag{3}$$

where the total strain $\boldsymbol{\varepsilon}$ and the thermal eigenstrain $\boldsymbol{\varepsilon}_T^e$ read as

$$\boldsymbol{\varepsilon} = \frac{1}{2}\left(\nabla\vec{u} + \nabla\vec{u}^T\right) \tag{4}$$

and

$$\boldsymbol{\varepsilon}_T^e = \alpha\Delta T\, \mathbf{1}, \tag{5}$$

respectively, with α and ΔT standing for the thermal expansion coefficient and the temperature change, respectively. The components of the second-order identity tensor $\boldsymbol{1}$ are equal to the Kronecker delta. The elastic energy density is decomposed into a positive part $\psi_e^+(\boldsymbol{\varepsilon_e})$ due to tension and a negative part $\psi_e^-(\boldsymbol{\varepsilon_e})$ due to compression. The positive part decreases with increasing cracking, i.e. [42–44]

$$\psi_e(\boldsymbol{\varepsilon_e}, \phi) = g(\phi)\,\psi_e^+(\boldsymbol{\varepsilon_e}) + \psi_e^-(\boldsymbol{\varepsilon_e}), \tag{6}$$

where $g(\phi)$ is the degradation function, reading as [42]

$$g(\phi) = (1-s)(1-\phi)^2 + s. \tag{7}$$

The parameter $s \ll 1$ is introduced to prevent the vanishing of the contribution of $\psi_e^+(\boldsymbol{\varepsilon_e})$ at $\phi = 1$, for the sake of computational robustness. The positive and negative parts of the elastic energy density read as [44]

$$\psi_e^\pm(\boldsymbol{\varepsilon_e}) = \frac{1}{2}\lambda\langle\varepsilon_{e,1} + \varepsilon_{e,2} + \varepsilon_{e,3}\rangle_\pm^2 + \mu\left(\langle\varepsilon_{e,1}\rangle_\pm^2 + \langle\varepsilon_{e,2}\rangle_\pm^2 + \langle\varepsilon_{e,3}\rangle_\pm^2\right), \tag{8}$$

with λ and μ standing for the bulk and shear modulus, respectively. $\varepsilon_{e,i}$ ($i = 1, 2, 3$) represents the counterpart of the principal elastic strain in the direction $\vec{n}_i$, i.e.

$$\boldsymbol{\varepsilon_e} = \sum_{i=1,2,3} \varepsilon_{e,i}\, \vec{n}_i \otimes \vec{n}_i. \tag{9}$$

The operators $\langle x\rangle_+$ and $\langle x\rangle_-$ are defined as

$$\langle x\rangle_+ = \frac{1}{2}(|x| + x), \quad \langle x\rangle_- = \frac{1}{2}(|x| - x). \tag{10}$$

The heat flux $\vec{q}$ is equal to the product of the thermal conductivity k_{eff} and the negative temperature gradient $-\nabla T$, i.e.

$$\vec{q} = -k_{eff}\nabla T. \tag{11}$$

Notably, the thermal conductivity decreases with increasing cracking. Following the phase-field regularization of discrete cracks into smeared damage, the effective conductivity is formulated with the phase-field damage variable ϕ, as [53]

$$k_{eff} = (1-\phi)^2\, k_0 + \phi^2\, k_c, \tag{12}$$

where k_0 is the thermal conductivity of the undamaged material body and k_c represents that of the crack phase, dominated by the filling medium. Considering the low thermal conductivity of air ($k_c \approx 0$), the effective conductivity reads as [54]

$$k_{eff} = (1-\phi)^2\, k_0. \tag{13}$$

The governing equations are established by substituting Eq. (7) into Eq. (6) and inserting the result, together with Eq. (2), into Eq. (1). This is followed by computing the variation of $\mathscr{L}$ due to variations of the displacement, the temperature, and the phase-field variable, i.e. of $\vec{u}$, T, and ϕ, respectively. The stationarity of $\mathscr{L}$ requires that its variation vanishes. This results in

$$\nabla\boldsymbol{\sigma} + \vec{b} = \rho\ddot{\vec{u}}, \text{ in } \Omega, \tag{14}$$

$$\rho c_p\dot{T} + \nabla\vec{q} = \Phi, \text{ in } \Omega, \tag{15}$$

$$\left[\frac{2l_0(1-s)\psi_e^+}{G_c} + 1\right](1-\phi) - l_0^2\Delta\phi = 1, \text{ in } \Omega, \tag{16}$$

with $\Delta = \nabla\cdot\nabla$ standing for the Laplace operator. The stress tensor $\boldsymbol{\sigma}$ is obtained as

$$\boldsymbol{\sigma} = \left[(1-s)(1-\phi)^2 + s\right]\frac{\partial\psi_e^+(\boldsymbol{\varepsilon_e})}{\partial\boldsymbol{\varepsilon_e}} + \frac{\partial\psi_e^-(\boldsymbol{\varepsilon_e})}{\partial\boldsymbol{\varepsilon_e}}. \tag{17}$$

In order to ensure the irreversibility of the crack propagation, a memory field of the strain energy density $\mathscr{H}$ is introduced as

$$\mathscr{H} = \begin{cases} \psi_e^+, & \psi_e^+ > \mathscr{H}_i \\ \mathscr{H}_i, & \psi_e^+ \leq \mathscr{H}_i \end{cases}, \tag{18}$$

with $\mathscr{H}_i$ denoting the maximum historical strain energy density in the previous load increments. Replacing ψ_e^+ in Eq. (16) by $\mathscr{H}$ according to Eq. (18) leads to the governing equation of the phase-field variable ϕ as

$$\left[\frac{2l_0(1-s)\mathscr{H}}{G_c} + 1\right](1-\phi) - l_0^2\Delta\phi = 1, \text{ in } \Omega. \tag{19}$$

The boundary conditions, see Fig. 1, read as

$$\begin{cases} \boldsymbol{\sigma}\cdot\vec{n} = \vec{t}, \text{ on } \partial\Omega_t \\ \vec{q}\cdot\vec{n} = q_\Gamma, \text{ on } \partial\Omega_q \\ \vec{u} = \vec{u}_\Gamma, \text{ on } \partial\Omega_u \\ T = T_\Gamma, \text{ on } \partial\Omega_T \\ \dfrac{\partial\phi}{\partial\vec{n}} = 0, \text{ on } \partial\Omega \end{cases}, \tag{20}$$

with $\vec{n}$ standing for the outward unit normal vector on the boundary $\partial\Omega$.

2.2. Mesoscale representation of concrete

The ITZs in the concrete, which are thin layers typically of a thickness ranging from 15 to 30 μm surrounding the aggregates, are considered as the weakest links inside the concrete microstructure due to their high porosity [55]. Consideration of the ITZs is crucial for the investigation of the initiation and propagation of microcracking in concrete. However, the small thickness of these layers presents numerical simulations with a great challenge. Following [50], an auxiliary phase-field $\eta(\vec{x})$ is introduced to regularize ultrathin ITZs to smeared interphases surrounding the aggregates, see Fig. 1(b). For simplicity, only coarse aggregates with diameters larger than 2 mm are considered in the following numerical simulations, while fine aggregates, along with the surrounding cement paste, are regarded as the mortar matrix.

The governing equation and the boundary conditions for the interfacial phase-field $\eta(\vec{x})$ are defined as follows [50]:

$$\begin{cases} \eta - l_i^2 \Delta\eta = 0, \text{ in } \Omega \\ \eta(\vec{x}) = 1, \text{ on } \Gamma_{ITZ} \\ \nabla\eta \cdot \vec{n} = 0, \text{ on } \partial\Omega \end{cases}, \tag{21}$$

with Γ_{ITZ} representing the aggregate boundaries and l_i denoting the length-scale parameter of the interfacial phase-field; l_i can be taken as equal to the length-scale parameter of the crack phase-field, i.e. $l_i = l_0$ [52]. The latter governs the regularization width of the smeared interphases. This regularization avoids direct resolution of the sub-millimetric width of the ITZs, amounting typically to some 40 microns [55], into the finite mesh. Instead, the mechanical behavior of the weak ITZs is preserved by energy-based homogenization. This allows for modeling the crack initiation and propagation at ITZs without ultrafine meshes. The equivalent critical energy release rate inside the smeared interphasial zone, $G_{c,s}(\eta)$, smoothly changes from that of mortar, $G_{c,mort}$, at $\eta = 0$, to that of ITZ, $G_{c,ITZ}$, at $\eta = 1$. It can be expressed as

$$G_{c,s}(\eta) = G_{c,ITZ}[1 - h(\eta)] + G_{c,mort} h(\eta), \tag{22}$$

with $h(\eta) = (1-\eta)^2$ following from [50]. Given that the critical energy release rate of the ITZ is smaller than that of mortar, i.e. $G_{c,ITZ} < G_{c,mort}$, Eq. (22) results in an overestimation of the energy dissipated due to interfacial cracking. To mitigate this, a generalized critical energy release rate, $\overline{G}_{c,ITZ}$, is introduced, which guarantees conservation of the fracture energy in the smeared crack zone [50]:

$$G_{c,ITZ} = \int_{-D_s}^{D_s} \{\overline{G}_{c,ITZ}[1 - h(\eta)] + G_{c,mort} h(\eta)\} \gamma_d(\eta, \nabla\eta) d\Omega. \tag{23}$$

The equivalent critical energy release rate inside the smeared interphasial zone $G_{c,s}$ is determined by inserting $\overline{G}_{c,ITZ}$, obtained from Eq. (23), into Eq. (22).

The size distribution of the aggregates in the concrete mixture is assumed to follow the Fuller grading curve, which is often used in engineering practice. The cumulative probability of the aggregates with diameters smaller than D_0 reads as

$$P(D < D_0) = \left(\frac{D_0}{D_{\max}}\right)^{0.5}, \tag{24}$$

where $D_{\max}$ represents the largest diameter of the aggregates. In order to reduce the computational efforts, the mesoscopic composition of concrete is simulated by representative two-dimensional elements. They can be established by cutting the three-dimensional medium of concrete with a plane. This results in a cross-section with intersection circles, representing coarse aggregates. The cumulative size distribution of these circles follows from the Walraven function [56,57] as

$$P(D < D_0) = 1.455\left(\frac{D_0}{D_{\max}}\right)^{0.5} - 0.500\left(\frac{D_0}{D_{\max}}\right)^{2} + 0.036\left(\frac{D_0}{D_{\max}}\right)^{4} + 0.006\left(\frac{D_0}{D_{\max}}\right)^{6} + 0.002\left(\frac{D_0}{D_{\max}}\right)^{8} + 0.001\left(\frac{D_0}{D_{\max}}\right)^{10}. \tag{25}$$

2.3. Model simplifications and limitations

While the proposed thermomechanical phase-field framework captures the essential elements of the fracture behavior of concrete, the following simplifications are made as to achieve a reasonable balance between computational costs and research focus:

- Concrete and its mesoscopic constituents (mortar, aggregates, and ITZs) are considered to be isotropic.
- The dynamic simulation of moisture transport during the diurnal temperature changes is beyond the scope of the present work. Instead, a stationary and uniform humidity field is envisioned. Still, different moisture levels are analyzed in order to account for seasonal variations [58]. The *RH*-dependent thermal expansion behavior is accounted for by means of Eq. (5).
- The ultrathin ITZs are represented by smeared interphasial phase-fields. Their actually graded thermomechanical properties remain unresolved in the interest of reasonable computation efforts.

While these simplifications indicate interesting directions for future extensions of the model, they are reasonable in relation to the focus of the present contribution, which rests on studying the influence of relative humidity on the thermal response of concrete structures.

3. Exemplary study of a thermally-loaded concrete plate

3.1. Numerical model

A concrete pavement slab is exemplarily analyzed, see Fig. 2. The slab is modeled as a two-dimensional plate with the thickness of $h = 0.25$ m and the length of $l = 5.00$ m, considering plane strain hypothesis. The plate is considered to rest on an elastic Winkler foundation, with the modulus of subgrade reaction amounting to 100 MPa/m. This value is representative for well-compacted sand and gravel [59,60].

The plate is subjected to daily temperature cycles. For simplicity, it is considered to be in an isothermal initial condition, characterized by a reference temperature of T_{ref}. The temperature at its bottom surface is assumed to be equal to the reference temperature, whereas the temperature at its top surface varies diurnally due to solar heating. The following function is introduced to describe this temperature variation after sunrise [4]:

$$T^{top} = T_{ref} + \Delta T_{fin}^{top} \cdot \frac{1}{2}\left[1 - \cos\left(\frac{t\pi}{12\,\text{h}}\right)\right], \tag{26}$$

with $T_{ref} = 17$ °C and $\Delta T_{fin}^{top} = 45$ °C, representing a typical scenario in

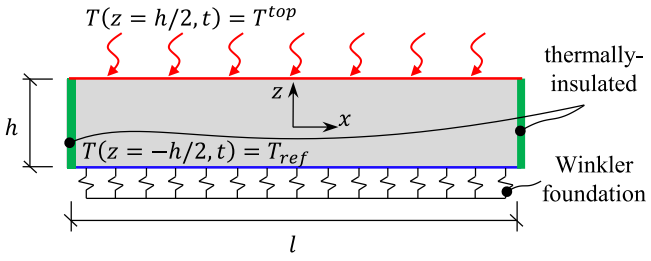

Fig. 2. Concrete plate, resting on a Winkler foundation, subjected to one-dimensional heat conduction in the thickness direction.

summer. The lateral surfaces are considered to be thermally-insulated, resulting in one-dimensional heat conduction along the thickness direction of the plate. The representative differential equation is given as

$$\frac{\partial T}{\partial t} - a\frac{\partial^2 T}{\partial z^2} = 0, \tag{27}$$

with the thermal diffusivity $a = k_0/(c_p\,\rho) = 0.85 \times 10^{-6}$ m^2/s for concrete [61]. For quantification of the temperature field, the concrete is considered to be heterogenous. The temperature is nonlinearly distributed in the thickness direction of the plate at the two investigated time instants, at 3 and 12 h after sunrise, see Fig. 3. Whereas, the internal relative humidity of concrete pavement is reported to be only slightly affected by diurnal ambient *RH* fluctuations, being predominantly governed by seasonal *RH* variations [58]. Therefore, the internal *RH* is considered as constant and uniform inside the plate herein, with *RH* = 50%, 65%, and 100%, respectively, chosen for the exemplary study to encompass typical service environments [1,58].

The thermomechanical response of the plate, considering the heterogeneity of concrete, is addressed by conducting a macroscopic and a mesoscopic phase-field analysis. Because of symmetry, only half of the structure is modeled in the numerical analyses. As for the *macroscopic* phase-field analysis, the plate is discretized into 5095 triangular elements, see Fig. 4. As for the *mesoscopic* phase-field analysis, the central 2 m-part of the plate, which is susceptible to thermal cracking, is modeled as a heterogeneous composite. It consists of mortar, coarse aggregates, and interfacial transition zones (ITZs), while, for computational efficiency, the concrete of the remaining part of the plate is treated as a homogeneous material. The largest and smallest diameter of the coarse aggregates is set as 16 mm and 2 mm, respectively, based on typical mixture designs of concrete. By referring to the Walraven function, see Eq. (25), the size distribution of the aggregates is quantified. The coarse circular aggregates are randomly distributed inside the mesoscopic part of the plate, as illustrated in Fig. 5. For the mesoscopic analysis, the plate is discretized into 199,856 triangular elements.

The investigated plate consists of mature concrete, made with ordinary Portland cement with an initial water-to-cement mass ratio of 0.40, coarse aggregates of basalt, and fine aggregates of sandstone. The mesoscale heterogeneity of concrete, modeled as spherical coarse aggregates embedded in a continuous mortar matrix with interfacial transition zones (ITZs) in-between, is investigated in the framework of the established mesoscale thermomechanical phase-field model. For simplicity, the mortar, consisting of cement paste, fine aggregates, and ITZs, is considered as homogeneous. Because of the small volume fraction of the ITZs, they can be idealized as two-dimensional interfaces in the homogenization [4,62,63]. The thermoelastic properties of the mortar and the concrete can be determined by means of the Mori-Tanaka scheme. The homogenized bulk modulus, k_{hom}, shear modulus, μ_{hom}, and

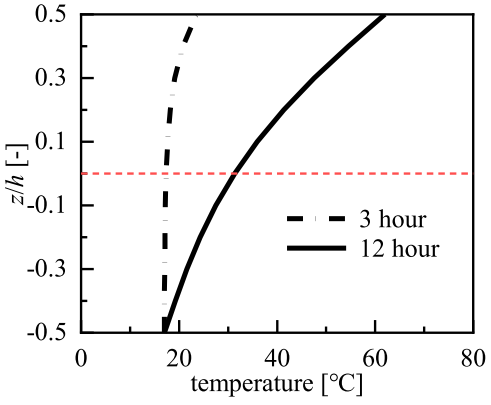

Fig. 3. Temperature distribution in the thickness direction of the plate at time instants of 3 h and 12 h after sunrise.

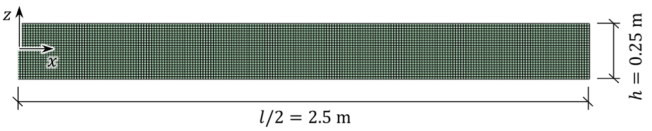

Fig. 4. Two-dimensional finite element mesh for the macroscopic phase-field analysis of the concrete plate.

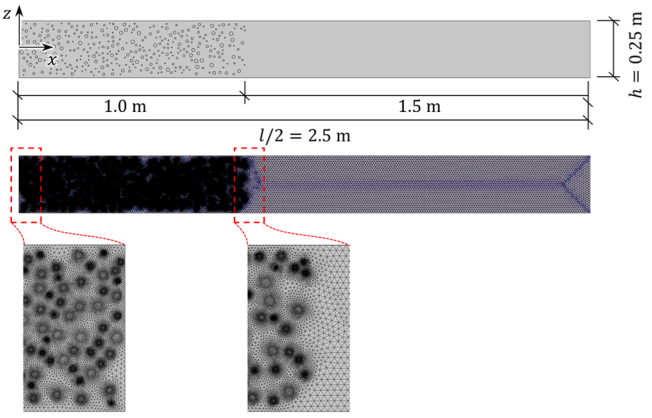

Fig. 5. Two-dimensional representation and finite element mesh for the mesoscopic phase-field analysis of the concrete plate.

thermal expansion coefficient, α_{hom}, of the matrix-inclusion composite are calculated as follows [15]:

$$k_{\text{hom}} = \frac{f_i k_i \left[1 + \frac{3(k_i - k_m)}{3k_m + 4\mu_m}\right]^{-1} + f_m k_m}{f_i \left[1 + \frac{3(k_i - k_m)}{3k_m + 4\mu_m}\right]^{-1} + f_m}, \tag{28}$$

$$\mu_{\text{hom}} = \frac{f_i \mu_i \left[1 + \frac{6(k_m + 2\mu_m)(\mu_i - \mu_m)}{5\mu_m(3k_m + 4\mu_m)}\right]^{-1} + f_m \mu_m}{f_i \left[1 + \frac{6(k_m + 2\mu_m)(\mu_i - \mu_m)}{5\mu_m(3k_m + 4\mu_m)}\right]^{-1} + f_m}, \tag{29}$$

and

$$\alpha_{\text{hom}} = \frac{3k_i k_m(\alpha_m f_m + \alpha_i f_i) + 4\mu_m(\alpha_m f_m k_m + \alpha_i f_i k_i)}{3k_i k_m + 4\mu_m(f_m k_m + f_i k_i)}, \tag{30}$$

where k_p, μ_p, α_p, and f_p ($p = i,m$) stand for the bulk modulus, the shear modulus, the thermal expansion coefficient, and the volume fraction of the inclusion and matrix phase, respectively. The corresponding Young's modulus and Poisson's ratio of the homogenized composite as well as its constituents are obtained as

$$E = \frac{9k\mu}{3k + \mu}, \upsilon = \frac{3k - 2\mu}{6k + 2\mu}, \tag{31}$$

holding for isotropic materials. The volume fraction of the aggregates is chosen as $f_{agg}^{con} = 0.70$. Aggregates with diameters smaller than 2 mm are considered as fine aggregates. The rest are coarse aggregates, the largest diameter of which is set equal to 16 mm. The volume fraction of the fine aggregates is determined from the Fuller grading curve, see Eq. (24), as $f_{fagg}^{agg} = (2/16)^{0.5} = 0.3535$. Thus, the volume fraction of the coarse aggregates follows as $f_{cagg}^{agg} = 1 - f_{fagg}^{agg} = 0.6465$. At first, the matrix-inclusion composite of mortar, containing fine aggregates and cement paste, is homogenized. The volume fractions of the fine aggregates and the cement paste, with respect to the volume of mortar, follow as

$$f_{fagg}^{mort} = \frac{f_{fagg}^{con}}{f_{cp}^{con} + f_{fagg}^{con}} = \frac{f_{agg}^{con} f_{fagg}^{agg}}{\left(1 - f_{agg}^{con}\right) + f_{agg}^{con} f_{fagg}^{agg}} = 0.452 \tag{32}$$

and

$$f_{cp}^{mort} = 1 - f_{fagg}^{mort} = 0.548. \tag{33}$$

The thermal expansion coefficient of cement paste and, thus, the ones of both mortar and concrete, depends nonlinearly on the internal relative humidity, see Fig. 6. The elastic properties of the mature cement paste and the thermoelastic properties of the fine sandstone aggregates are listed in Table 1(a) concerning the input and the homogenization results for mortar. Specifically, Young's modulus of the cement paste follows from the experimental results in [64], for samples with an initial water-to-cement mass ratio of 0.40, at the age of 56 days after mixing. Its Poisson's ratio is considered to be constant and equal to 0.20 [15]. The thermoelastic properties of the aggregates mainly depend on the mineral composition which may vary with the porosity, crystal orientation, and texture. Therefore, averages of the listed ranges for the thermal expansion coefficients [14] and the elastic parameters [65] for typical rock aggregates are considered, see [15] for details. Thereafter, the matrix-inclusion composite of concrete, containing coarse aggregates and homogenized mortar, is homogenized. The volume fractions of the coarse aggregates and the homogenized mortar, with respect to the volume of concrete, follow as

$$f_{cagg}^{con} = f_{agg}^{con} f_{cagg}^{agg} = \left(1 - f_{fagg}^{con}\right) f_{agg}^{con} = 0.453 \tag{34}$$

and

$$f_{mort}^{con} = 1 - f_{fagg}^{mort} = 0.547. \tag{35}$$

The thermoelastic properties of the coarse basalt aggregates follow from [15], depending on the mineral composition, see Table 1(b) for the input and the homogenization results. The critical energy release rate of concrete is taken as $G_{c,con} = 100\ \mathrm{J/m^2}$ [66]. Following [67], the corresponding values for the mortar and the ITZs are chosen as $G_{c,mort} = 72\ \mathrm{J/m^2}$ and $G_{c,ITZ} = 21\ \mathrm{J/m^2}$, respectively. Given that the aggregates of normal-strength concrete are stronger than the mortar and the ITZs, the former are considered to remain elastic [67]. Young's modulus of the ITZs is considered to amount to 85 % of that of the surrounding bulk matrix, i.e. $E_{ITZ} = 0.85E_{mort} = 23.94$ GPa, whereas their Poisson's ratios and thermal expansion coefficients are considered to be equal, i.e. $\upsilon_{ITZ} = \upsilon_{mort}$ and $\alpha_{ITZ} = \alpha_{mort}$ [4], see Table 1 for the corresponding values.

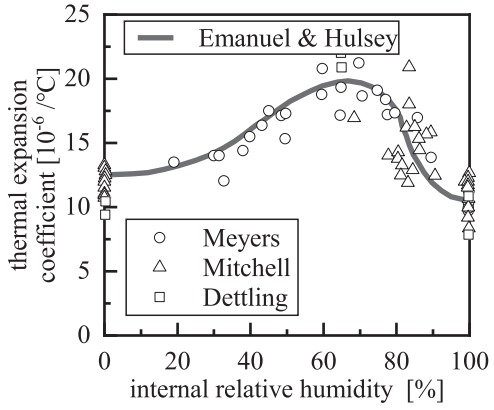

Fig. 6. Dependence of the thermal expansion coefficient of the cement paste on the internal relative humidity, with test data from Meyers [68], Mitchell [69], Dettling [70], and a fitting curve from Emanuel and Hulsey [14], after [21].

3.2. Results of macroscopic phase-field analysis

The distribution of the macroscopic normal stresses, experienced by concrete at the two investigated time instants, is nonlinear in the thickness direction of the plate, see Fig. 7 for the results at the midsection of the plate. The midsection is considered to be representative of the bulk slab response, avoiding the influence of edge effects. Compressive stresses are observed near both the top and the bottom surface of the plate, while tensile stresses dominate the central region. As the time progresses from 3 h to 12 h after sunrise, the stresses increase significantly. However, the influence of the internal relative humidity on the macroscopic stresses is relatively small. This is primarily due to the rather moderate effect of the relative humidity on the thermal expansion coefficient of concrete, see Table 1. The thermal expansion behavior of cement paste is highly sensitive to changes in *RH*, see Fig. 6, but cement paste occupies only some 30 % of the concrete volume, while the rest of the volume is occupied by sand and aggregates which have an *RH*-independent thermal expansion behavior. Specifically, 3 h after sunrise, the largest compressive stress at the top surface amounts to 2.14 MPa, 2.25 MPa, and 1.79 MPa for $RH = 50\%$, 65%, and 100%, respectively, and the corresponding largest tensile stress in the central region amounts to 0.45 MPa, 0.47 MPa, and 0.37 MPa, respectively. 12 h after sunrise, the largest compressive stress at the top surface increases to 4.12 MPa, 4.26 MPa, and 3.67 MPa for $RH = 50\%$, 65%, and 100%, respectively, and the corresponding largest tensile stress in the central part of the plate increases to 1.39 MPa, 1.47 MPa, and 1.21 MPa, respectively. The macroscopic phase-field results referring to 12 h after sunrise agree well with the reported analytical solutions computed based on the Kirchhoff hypothesis and a Vlasov-type of structural analysis [4], subjected to the same thermal loading, see Fig. 7(b). The quantified tensile stresses are smaller than the tensile strength of concrete, indicating that the analyzed diurnal temperature increase is unlikely to induce macroscopic cracking.

The distributions of the phase-field damage, ϕ, inside the concrete plate at the two investigated time instants are illustrated in Fig. 8. Overall, the damage remains almost negligible, with the maximum values reading as $\phi = 12.35 \times 10^{-6}$ and 18.02×10^{-5} at the time instants 3 h and 12 h after sunrise, respectively. The phase-field damage is similarly distributed as the macroscopic tensile stresses. At both time instants, the phase-field damage of the plate at $RH = 65\%$ is slightly larger than that of the plate at $RH = 50\%$ and $RH = 100\%$. This follows from the slightly larger thermal expansion coefficient and, thus, from the larger macroscopic tensile stresses. It is concluded that the influence of relative humidity on the macroscopic stresses and damage of the concrete plate, subjected to a characteristic diurnal temperature change, is rather small.

3.3. Results of mesoscopic phase-field analysis

Distributions of the normal stresses, considering the mesostructural heterogeneity of concrete, generally follow a similar pattern as the one resulting from macroscopic analyses, see Fig. 9. The plate is generally subjected to compressive stresses near the top and bottom surfaces, whereas tensile stresses dominate in the central region. Both the tensile and compressive stresses increase as the time proceeds from 3 h to 12 h after sunrise. However, mesoscopic stress distributions exhibit significant mesoscopic variations, primarily due to the heterogeneity of concrete. At this scale, the *RH*-dependent mismatch of the thermal expansion coefficients between mortar and coarse aggregates is pronounced, see Table 1, leading to substantial local stress fluctuations. In the vicinity of the top surface, where the macroscopic concrete stresses are compressive, the coarse aggregates experience larger compressive stresses than the surrounding mortar. At $RH = 65\%$ and 50%, these stresses of the aggregates may even change from compressive to tensile. Conversely, in the central region of the plate, where the macroscopic

Table 1
Input and homogenization results of the thermoelastic properties for (a) mortar, and (b) concrete.

(a) mortar						
materials	volume fraction [-]	Young's modulus [GPa]	Poisson's ratio [-]	thermal expansion coefficient [10^{-6}/°C]		
				RH = 50%	RH = 65%	RH = 100%
fine aggregates	0.452	35.00	0.25	11.25		
cement paste	0.548	23.60	0.20	18.00	20.20	10.50
mortar	-	28.17	0.22	14.53	15.60	10.89
(b) concrete						
materials	volume fraction [-]	Young's modulus [GPa]	Poisson's ratio [-]	thermal expansion coefficient [10^{-6}/°C]		
				RH = 50%	RH = 65%	RH = 100%
coarse aggregates	0.453	70.00	0.22	6.75		
mortar	0.547	28.17	0.22	14.53	15.60	10.89
concrete	-	41.63	0.22	10.37	10.86	8.67

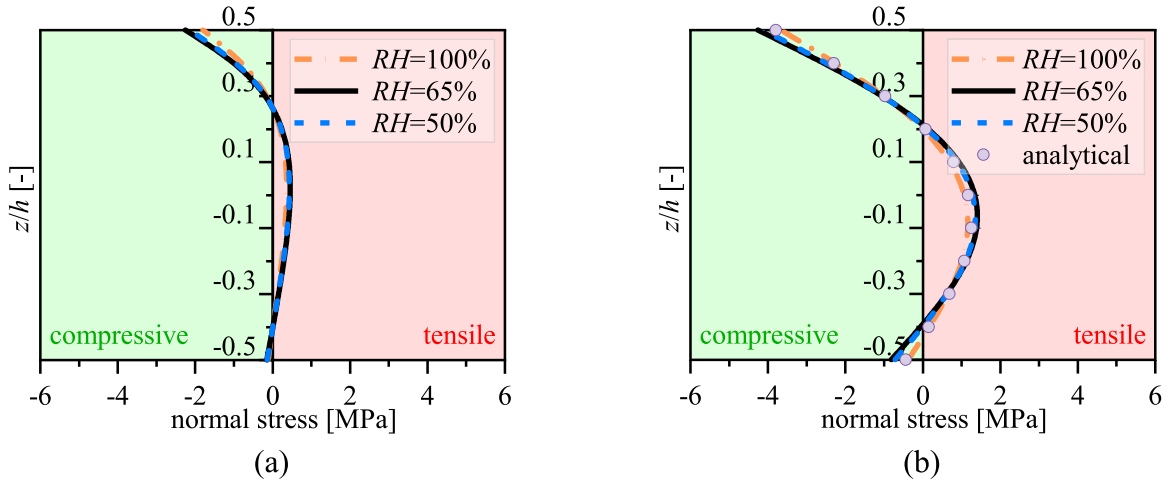

Fig. 7. Distribution of the macroscopic normal stresses across the thickness at the midsection of the plate, at the time instants of (a) 3 h and (b) 12 h after sunrise, with the latter being compared with the analytical solutions for these stresses in [4].

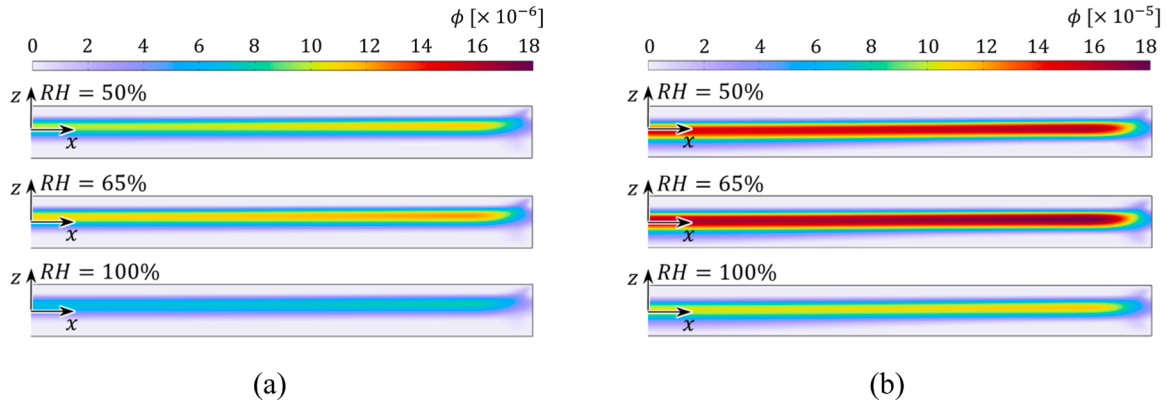

Fig. 8. Distribution of the phase-field damage, ϕ, of the plate at the time instants of (a) 3 h and (b) 12 h after sunrise.

concrete stresses are tensile, the aggregates experience larger tensile stresses than the surrounding mortar. Notably, these stress differences are most pronounced at RH = 65%, which is attributed to the largest thermal expansion coefficient across all values of relative humidity. The stresses experienced by the aggregates are transferred to the mortar through the interfacial transition zones (ITZs).

Because of the significant fluctuations of the material properties and the mesoscopic stresses, mesoscopic cracks are observed in the concrete plate subjected to the analyzed diurnal temperature change, see Fig. 10. The local phase-field damage, ϕ, is much larger than that obtained from macroscopic phase-field analyses. 3 h after sunrise, the maximum phase-field damage reaches $\phi = 12.45 \times 10^{-3}$ for RH = 65%. 12 h after sunrise, the maximum phase-field damage reaches the magnitude of 1.0 for all three values of relative humidity, indicating mesoscopic cracking. Both the distribution and the density of the cracks are significantly influenced by the relative humidity. In the central region of the plate, where the macroscopic concrete stresses are tensile, mesoscopic cracks occur for all three relative humidity scenarios. They start at the ITZs and primarily propagate in the vertical direction around the aggregates, with some cracks penetrating into the surrounding mortar matrix which is also subjected to tensile stresses. For RH = 100%, fewer cracks are observed, while for RH = 65% and 50%, the crack density is

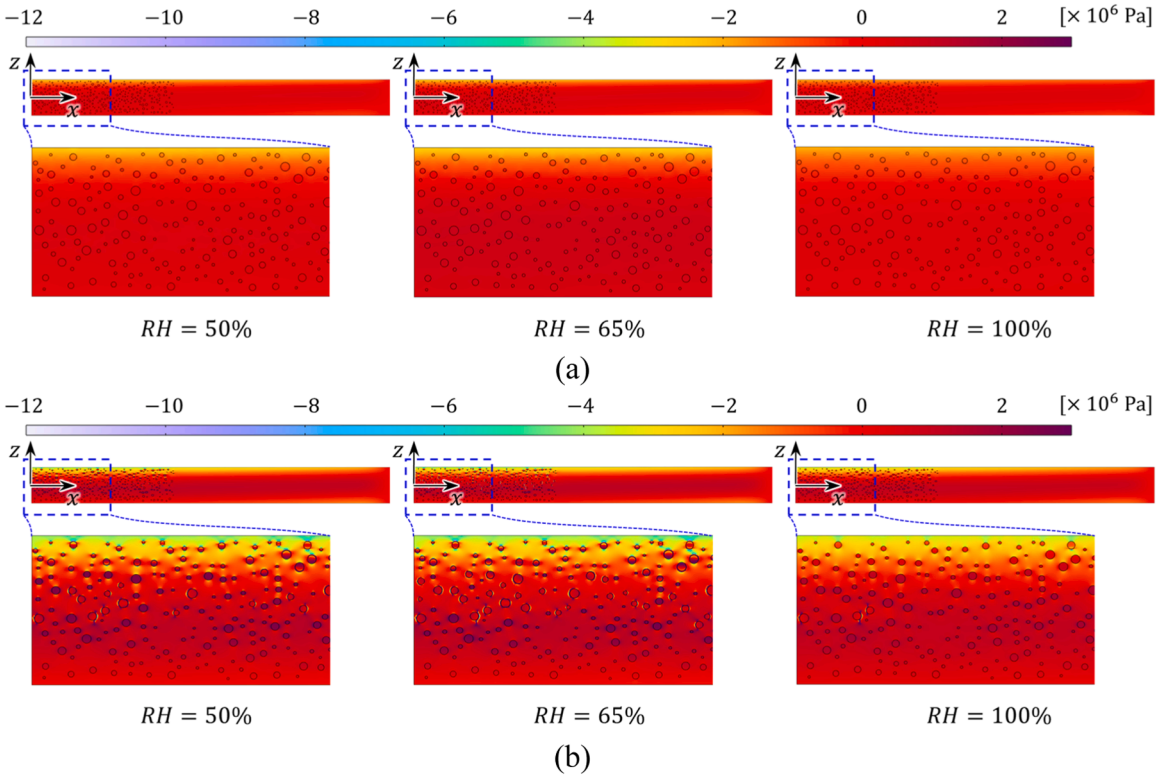

Fig. 9. Distribution of the normal stresses of the plate at the time instants of (a) 3 h and (b) 12 h after sunrise, considering the mesoscopic heterogeneity of concrete.

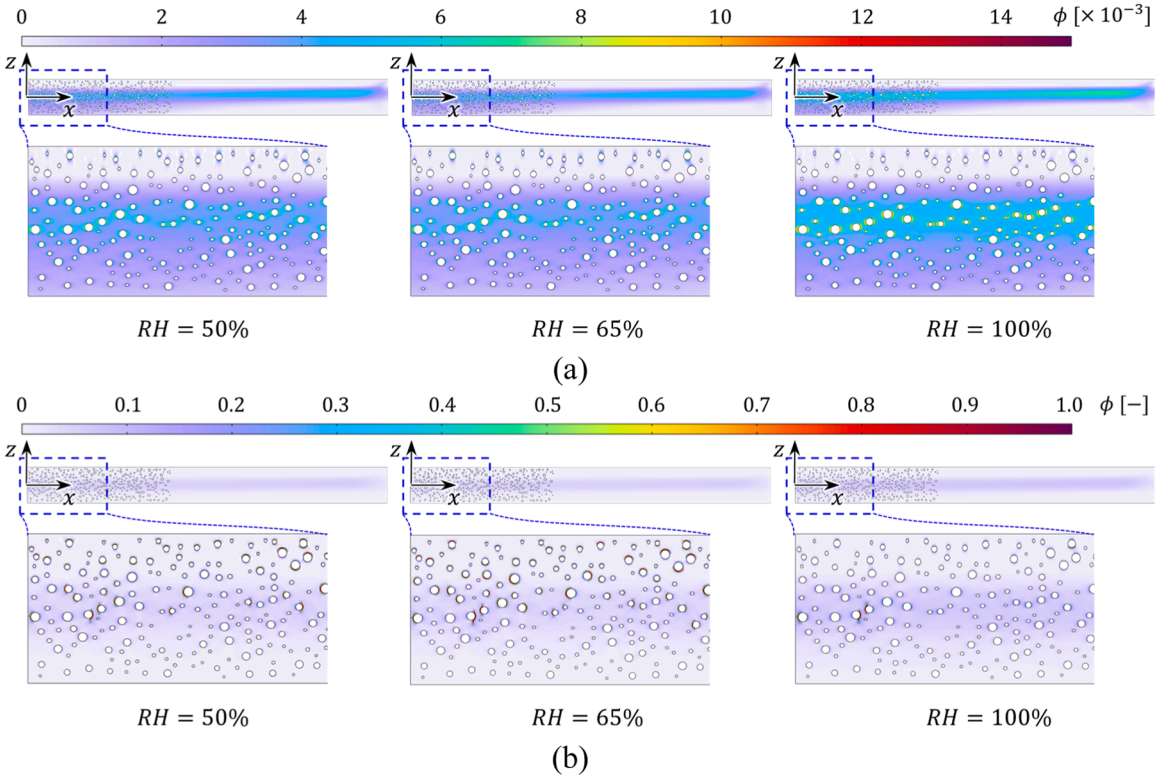

Fig. 10. Distribution of the phase-field damage, ϕ, of the plate at the time instants of (a) 3 h and (b) 12 h after sunrise, considering the mesoscopic heterogeneity of concrete; the color bar in (a) represents $\phi \times 10^{-3}$ to visualize small damage values while the color bar in (b) represents ϕ.

considerably larger. Surprisingly, even in the region near the top surface of the plate, where the macroscopic concrete stresses are compressive, mesoscopic cracking is observed for $RH = 65\%$ and 50%. In this region, cracks start at the ITZs in the horizontal direction and propagate circumferentially between the aggregates and the surrounding mortar, similarly as reported in [71]. These cracks remain inside the ITZs, since the surrounding mortar experiences compressive stresses.

4. Discussions

4.1. Fluctuation of mesoscopic stresses

The analyzed stress distribution of the mesoscopic phase-field simulation generally follows a pattern similar to that of the macroscopic phase-field simulation, while capturing significant local stress fluctuations. For an explicit comparison, these stress distributions are presented at a selected cross-section close to the midsection ($x = 0.067$ m), which is a boundary of the simulated half-plate, see Fig. 11. This cross-section is considered to be representative of the response of

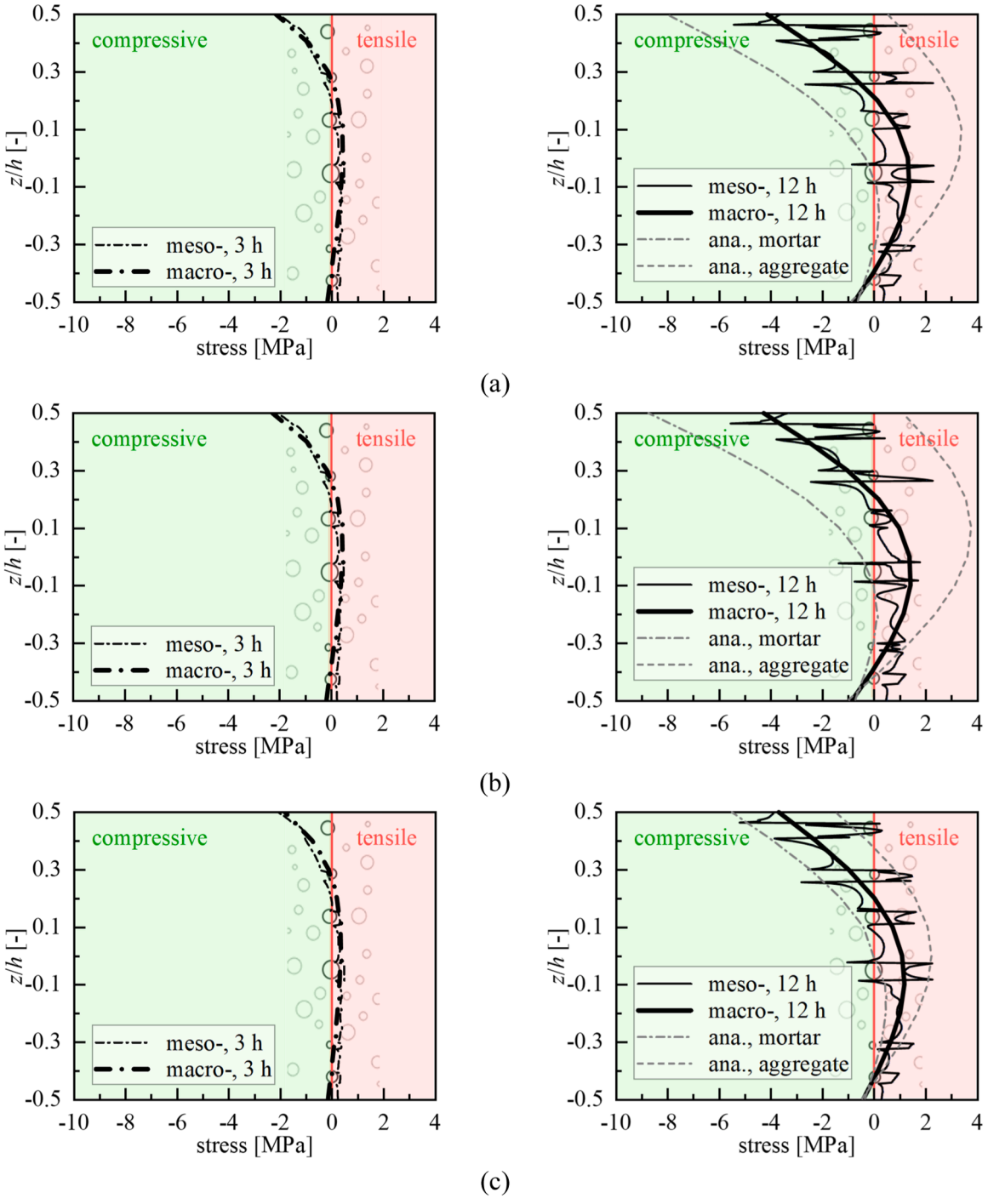

Fig. 11. Comparison of the macroscopic stresses and the mesoscopic stresses at the time instants of 3 h and 12 h after sunrise for (a) $RH = 50\%$, (b) $RH = 65\%$, and (c) $RH = 100\%$ at a cross-section close to the midsection ($x = 0.067$ m), with the 12-hour results being validated against analytical microelastic solutions.

the slab, capturing the heterogeneous stress distributions. The mesoscopic stresses, accounting for the heterogeneity of concrete, tend to fluctuate around the macroscopic stresses, strongly depending on the spatial distribution of the concrete constituents. At the interphases between the coarse aggregates and the surrounding mortar, abrupt stress variations are observed. They are attributed to the mismatch of the thermoelastic properties between the two phases. Specifically, the heated mortar, with its larger thermal expansion coefficient, experiences larger expansive thermal eigenstrains, compared to the embedded coarse aggregates. This disparity results in tension of the mortar and compression of the coarse aggregates. Furthermore, the stiffer coarse aggregates take a larger portion of the macrostresses, which can either accentuate or counteract the stress differences between the two phases.

The relative humidity is found to significantly influence the mesoscopic stresses as a result of its impact on the thermal expansion coefficient of mortar. For example, the uppermost coarse aggregate in the illustrated cross-section exhibits compressive stresses for $RH = 100\%$, see Fig. 11(c). However, for $RH = 50\%$ and 65%, the same aggregate experiences tensile stresses, see Fig. 11(a) and (b). This is attributed to the enhanced thermal expansion coefficient of partially-saturated mortar, leading to increased compression in the mortar and corresponding tension in the embedded coarse aggregates. As for the macroscopic stresses, the influence of the relative humidity is less pronounced, since the thermal expansion coefficient of concrete does not change much. This is attributed to the large volume fraction of the coarse aggregates, see Table 1. These findings highlight the importance of considering the heterogeneity of concrete in the computation of the stress distribution and its dependence on the relative humidity, especially in regions with a high potential of cracking.

Direct experimental validation of the mesoscopic stresses remains unfortunately impossible, as existing techniques, e.g. DIC [72], measure surface strains rather than internal mesostresses. As a remedy, the presented concept is validated by comparing the mesoscopic phase-field results with analytical results calculated in the context of a microelasticity approach, see the Appendix for details. Based on the macroscopic stresses and the temperature of concrete, the mesostresses of mortar and of the coarse aggregates are exemplarily quantified at 12 h after sunrise. It turns out that the mesostresses obtained with the numerical phase-field approach mostly fluctuate between the analytically computed mesostresses of mortar and aggregates, see Fig. 11. Particularly good agreement is observed for $RH = 100\%$, see Fig. 11(c), because the phase-field approach indicates minimal mesocracking and this implies that an elastic analysis is also realistic. At $RH = 65\%$ and 50%, however, the analytical microelastic stresses are larger than those obtained with the mesoscopic phase-field approach. This is attributed to the stress redistribution induced by mesocracking, which is accounted for in the phase-field model.

4.2. Pattern of mesoscale cracking

In the central region of the plate, where the macroscopic concrete stresses are tensile, the mesoscale cracking pattern is characterized by cracks initiating from the ITZs, some of which may propagate into the adjacent mortar. These cracks predominantly propagate in the vertical direction, see Fig. 10. The cracking mechanism is surprisingly complex in the upper region of the plate, where the macroscopic concrete stresses are compressive. There, horizontal cracks are observed inside the ITZs, see Fig. 10. This can be attributed to the mesoscopic stress states of concrete, as illustrated in Subsection 4.1. Specifically, the mortar in the central part of the plate experiences mesoscopic tensile stresses, which underlines the risk of cracking. Conversely, the mortar is in compression near the top surface of the plate, while the coarse aggregates can experience tensile stresses. These aggregates are considered to remain elastic in the present simulations. The stress difference between the mortar and the aggregates is transferred through the ITZs. The stress state of the ITZs varies with the position relative to the coarse aggregates, which determines the predominant orientation of the cracks.

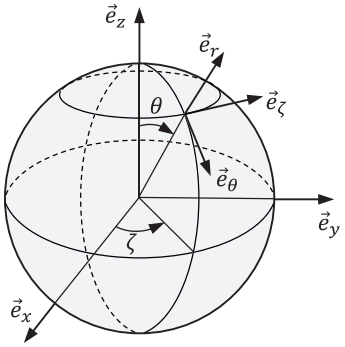

Fig. 12. Local spherical coordinate system referring to the coarse aggregates.

The stress states inside the ITZs of concrete can be determined analytically in the framework of micromechanics [4], based on the obtained macroscopic stress states and the temperature change of the concrete. A local spherical coordinate system with zenith angle θ and azimuth angle ζ is introduced to describe positions in the ITZs covering the spherical aggregates, see Fig. 12.

The stress states of the ITZs covering the coarse aggregates, located at the top surface and at the center of the midsection of the plate, defined by the coordinates $(x, z) = (0,\ 0.125)$ and $(x, z) = (0,\ 0)$, respectively, are exemplarily analyzed at 12 h after sunrise. The corresponding maximum principal normal stresses are computed, following the Appendix. They govern cracking of the ITZs. The largest value for $\zeta \in [0,\ 2\pi]$ along the meridian, i.e. as functions of the zenith angle θ, are illustrated as Fig. 12. At the center of the plate, the maximum principal normal stress exhibits an extreme value at $\theta = \pi/2$, see Fig. 13(b), underscoring the high risk of vertical tensile cracks in the ITZ in the equatorial regions of the aggregates. These cracks may also propagate into the surrounding mortar, which concurrently experiences tensile stresses. However, at the top surface of the plate, the maximum value of the largest principal normal stress occurs at $\theta = 0$, indicating that tensile cracking of the ITZs is likely to start in the polar regions of the aggregate in the horizontal direction, see Fig. 13(a). Due to the compressive stresses in the surrounding mortar and the high strength of the coarse aggregates, these cracks stay within the ITZs.

4.3. Sensitivity analyses

The aforementioned results indicate limited influence of the *RH*-dependent mesoscopic heterogeneity on the macroscopic thermomechanical response of the concrete plate. A parametric study is carried out in the following in order to demonstrate the influences of the height of the plate, of the interaction of the plate with its subgrade, and of the type of aggregates.

4.3.1. Sensitivity analysis regarding the height of the plate

In order to study the macroscopic thermomechanical response of plates with different geometric dimensions, the height of the plate is increased from 0.20 m to 0.25 m and further to 0.30 m. The internal relative humidity is kept constant at 65 %. The other input quantities are the same as in Section 3.

The distributions of the macroscopic normal stresses across the thickness of the plates with different heights are qualitatively similar, when the vertical coordinate is normalized by the height of the plate, see Fig. 14. There are compressive stresses near the top and the bottom surface of the plate. In the central region, there are tensile stresses. Still, there are quantitative differences. The larger the height of the plate, the larger the macroscopic normal stresses in most parts of the cross-section. Specifically, 12 h after sunrise, the largest compressive stress at the top surface amounts to 3.44 MPa for $h = 0.20$ m and to 5.34 MPa for $h =$

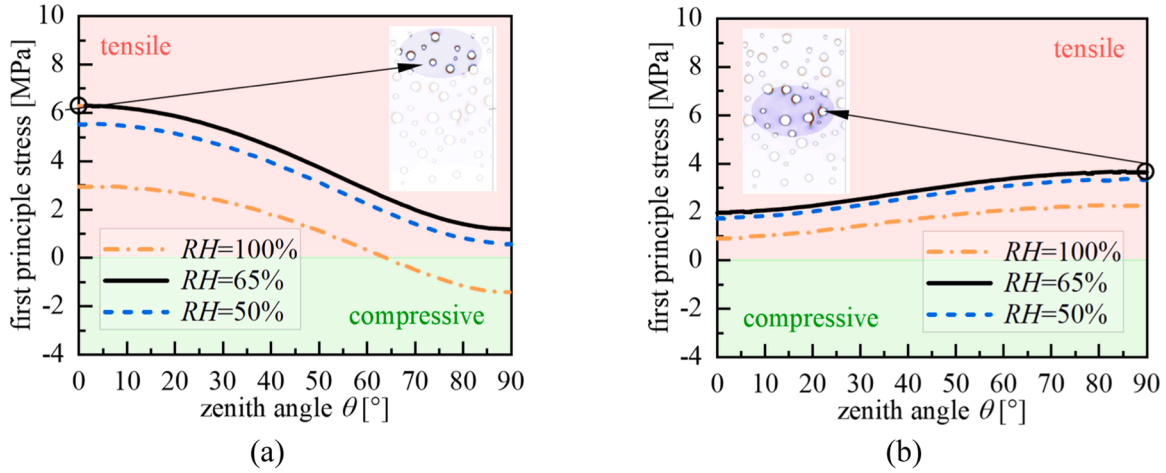

Fig. 13. Distribution of the largest first principal normal stresses of the ITZs covering the coarse aggregates at (a) the top surface, and (b) the center of the midsection of the plate at 12 h after sunrise.

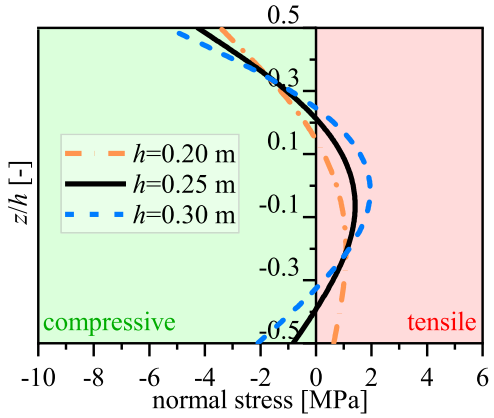

Fig. 14. Sensitivity analysis regarding the height of the plate: macroscopic normal stresses across the thickness at the midsection of the plate, at the time instant of 12 h after sunrise.

0.30 m, while the largest tensile stress in the central part of the plate is equal to 1.11 MPa in the former case and equal to 2.04 MPa in the latter case. This is mainly attributed to the prevented eigendistortion of the plate generators, which increases with increasing height of the plate [61].

4.3.2. *Sensitivity analysis regarding the interaction of the plate with the subgrade*

In order to study the influence of the stiffness of the subgrade on the macroscopic thermomechanical response of the plate, including consideration of the vertical support and the horizontal friction, a sensitivity analysis is conducted. Following the framework of [4], the thermal eigenstrain distribution across the height of the plate, induced by the temperature change, can be decomposed into a linear and a nonlinear part. They are related (i) to the eigenstretch and the eigencurvature of the plate as well as (ii) to the eigendistortion of the plate generators. The total thermal stress, σ_{tot}, is the sum of stress contributions resulting from the two eigenstrain portions, i.e.

$$\sigma_{tot} = \sigma_{lin} + \sigma_{non}, \tag{36}$$

where σ_{lin} represents the stress resulting from the *constrained* eigenstretch ε_0^e and eigencurvature κ_0^e of the plate, and σ_{non} represents the stress resulting from eigendistortion of the plate generators, which is prevented according to the Kirchhoff hypothesis, stating that the plate generators remain straight even under thermomechanical loading. Thus,

$$\sigma_{non} = -\frac{E_{con}}{1-\nu_{con}}\left(\alpha_{con}\Delta T - \varepsilon_0^e - \kappa_0^e z\right), \tag{37}$$

with E_{con}, ν_{con}, and α_{con} denoting Young's modulus, Poisson's ratio, and the thermal expansion coefficient of concrete. The stress contribution σ_{lin} depends on the slab-subgrade interaction. For the adopted Winkler foundation in this study, σ_{lin} is quantified by subtracting σ_{non}, computed by Eq. (37), from σ_{tot}, taken from Fig. 7. To capture uncertainties of the slab-subgrade interaction, σ_{lin} is varied by ±25% in the present sensitivity analysis. This is motivated by [73,74], where replacing the frictionless Winkler foundation with a Pasternak foundation, including horizontal friction, led to changes of the thermal stress from 1 % to 25%. The ±25% range is, therefore, taken as a conservative estimate to explore the potential influence of subgrade interaction, without directly implementing the Pasternak foundation and friction between the plate and the subgrade. The internal relative humidity is kept constant at 65 %. The other input quantities are the same as in Section 3.

The variation of σ_{lin} by ±25%, as illustrated by the blue-shaded area in Fig. 15, results in minor changes of the total thermal stress, as illustrated by the gray-shaded area in Fig. 15. The maximum compressive stress at the top surface changes by less than 10 %, i.e. from 4.26 MPa to 3.85 MPa and to 4.66 MPa, respectively. The maximum tensile stress in the central region changes by less than 4 %, i.e. from 1.47 MPa to 1.43 MPa and to 1.52 MPa, respectively. These small variations are

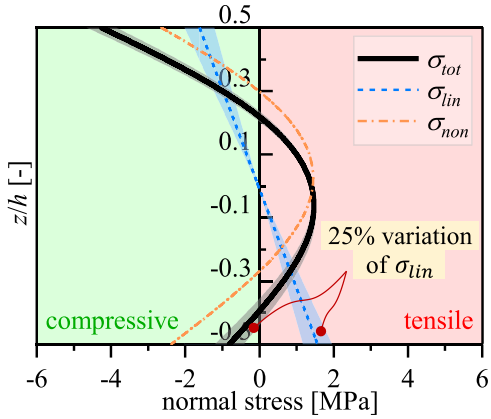

Fig. 15. Sensitivity analysis regarding the slab-subgrade interaction with ± 25% variation of σ_{lin}: macroscopic normal stresses across the thickness at the midsection of the plate, at the time instant of 12 h after sunrise.

attributed to the dominant contribution of the prevented eigendistortion, i.e. the nonlinear part of the temperature change across the height of the plate [4,75], which accounts for 79.3–95.2 % of the maximum tensile stress across the ±25% variation in σ_{lin}, see the dash-dotted line in Fig. 15. The influence of the subgrade-slab interaction on the thermal stress is insignificant when compared to the one of the plate height and the temperature nonlinearity [76–78]. Regardless of the subgrade-slab interaction, the risk of *macro*scopic tensile cracking of a plate subjected to the assumed thermal loading remains low. However, the mesoscopic heterogeneity of concrete significantly increases the risk of localized *meso*cracking.

4.3.3. Sensitivity analysis regarding the aggregate type

In order to study the role of the aggregate type, the coarse basalt aggregates are replaced by coarse quartzite aggregates, which is also frequently used. The internal relative humidity is kept constant at 65%. The thermoelastic properties of the coarse aggregates and of the corresponding concretes are summarized in Table 2. The other input quantities are the same as in Section 3.

The macroscopic normal stresses across the thickness of the plates are virtually the same for concrete made of coarse basalt and quartzite aggregates, see Fig. 16. This follows from the dominant contribution of the stress resulting from the prevented eigendistortion of the plate generators, σ_{non}, which is proportional to $E_{con}\alpha_{con}/(1-\nu_{con})$. For basalt and quartzite concretes, this value reads as 579.6×10^{-6} GPa/°C and 623.1×10^{-6} GPa/°C, respectively, leading to a similar distribution of the macroscopic stresses, see Fig. 16. This demonstrates the moderate dependence of the *macro*scopic global response on the properties of the aggregates. However, the *meso*scopic response is highly sensitive to the aggregate type. The thermal expansion coefficient of quartzite aggregates is much closer to that of the mortar than that of basalt aggregates. This reduces the mismatch of the mesoscopic thermal eigenstrains and, thus, of mesostress fluctuations. It results in a much lower crack density in quartzite concrete, compared to basalt concrete, see the mesoscopic cracking patterns in Fig. 16. This underlines the importance of mesoscale modeling to capture localized damage, even when the global responses are quite similar. For practical design, aggregates with thermal expansion coefficients close to that of mortar are recommended, in order to mitigate the risk of mesoscopic cracking.

5. Conclusions

In this study, the thermomechanical response and the cracking behavior of a concrete plate were investigated, with the focus on the influence of the internal relative humidity. The results of macroscopic and mesoscopic phase-field analyses were compared. Based on these results, the following conclusions are drawn:

- The relative humidity has a relatively small influence on the distribution of the macroscopic stresses experienced by the concrete, with the maximum tensile stress at the midsection of the plate reading as 1.39 MPa at $RH = 50\%$, 1.47 MPa at $RH = 65\%$, and 1.21 MPa at $RH = 100\%$. However, it significantly influences the mesoscopic stresses, experienced by the aggregates, the ITZs, and the mortar matrix. The local mesoscopic stresses fluctuate considerably because of the heterogeneous nature of concrete. It strongly depends on the relative humidity, because the thermal expansion coefficient of mortar is a nonlinear function of *RH*. For $RH = 65\%$, the thermal expansion coefficients of the mortar and the coarse aggregates differ most, leading to pronounced mesoscopic stress fluctuations that contribute to mesoscopic cracking.
- An interesting and somewhat surprising finding is that tension-induced mesoscopic cracking can even occur in regions which experience macroscopically *compressive* stresses. This effect is governed by local mesoscopic stress states of the concrete constituents. When heated, the expansive thermal eigenstrains in the mortar exceed those of the coarse aggregates. This results in tensile mesoscopic stresses of the aggregates and the surrounding ITZs, which might even be larger than the macroscopic compressive stress experienced by concrete. This highlights the complex and partially counterintuitive nature of the mesoscopic cracking behavior of thermally-loaded concrete.
- Mesoscopic cracking of concrete typically starts inside the ITZs, with the location, orientation, and propagation governed by the principal stress states. In this study, mesoscopic cracks were found to primarily develop (i) horizontally around the aggregates in the region of the top surface of the plate, where macroscopic compressive concrete stresses prevail, and (ii) vertically in the central part of the plate, where macroscopic tensile concrete stresses prevail. It was found that mesoscopic crack initiation can be predicted by using both mesoscale phase-field numerical simulations and microelastic models, providing insight into high-risk regions for cracking.
- Sensitivity analyses reveal that the height of the plate has a much greater influence on macroscopic thermal stresses than the slab-subgrade interaction. Increasing the height from 0.20 m to 0.30 m results in an increase of the maximum tensile stress at the midsection from 1.11 MPa to 2.04 MPa. The type of the coarse aggregate, affecting the *meso*scopic heterogeneity, has a minor influence on the *macro*stresses. However, it significantly influences *meso*cracking as the result of a mismatch of mesoscopic thermal eigenstrains.
- The mentioned findings underscore the necessity to account for the material heterogeneity and relative humidity in the analysis and the design of concrete structures subjected to thermal loading. Even regions where concrete experiences compressive stresses are susceptible to mesoscopic tension-induced cracking. This highlights the importance of quantifying mesoscopic stress and strain distributions across the concrete constituents in design and durability assessment of concrete structures.

Finally, it is noted that, while the macroscopic and mesoscale phase-field results have been compared with existing analytical solutions in this study, comprehensive experimental validation remains an open

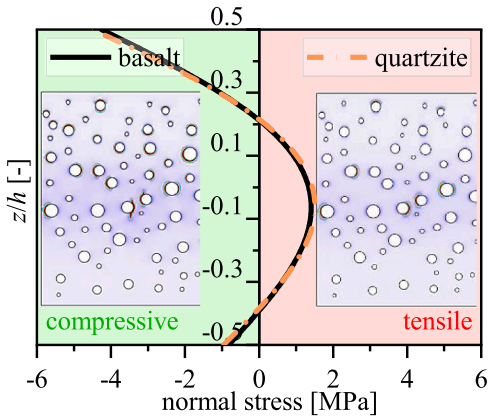

Fig. 16. Sensitivity analysis regarding the aggregate type: macroscopic normal stresses across the thickness at the midsection of the plate and mesoscopic cracking patterns, at the time instant of 12 h after sunrise.

Table 2
Thermoelastic properties of the basalt and quartzite coarse aggregates [15] and of the corresponding concretes, with E, ν, and α denoting Young's modulus, Poisson's ratio, and the thermal expansion coefficient, respectively.

aggregate	E_{agg} [GPa]	ν_{agg} [-]	α_{agg} [10^{-6}/°C]	E_{con} [GPa]	ν_{con} [-]	α_{con} [10^{-6}/°C]
basalt	70.00	0.22	6.75	41.63	0.22	10.86
quartzite	50.00	0.16	11.75	36.36	0.20	13.71

topic. The present framework can serve as a guideline for designing innovative and at least partly destructive field testing protocols, indicating the need for precise measurements of temperature and *RH* fluctuations as well as of macroscopic and mesoscopic stresses and strains, crack initiation, and crack propagation.

CRediT authorship contribution statement

Hui WANG: Writing – original draft, Methodology, Investigation, Conceptualization. **Luyao LIU**: Writing – original draft, Visualization, Investigation. **Xi CHEN**: Investigation. **Wei JIANG**: Software, Investigation. **Herbert A. MANG**: Writing – review & editing. **Bernhard PICHLER**: Writing – review & editing, Conceptualization.

Declaration of Competing Interest

The authors declare that they have no known competing financial interests or personal relationships that could have appeared to influence the work reported in this paper.

Acknowledgement

The first author gratefully acknowledges financial support by the National Natural Science Foundation of China (Grant No. 52208398 and 52478401). The authors acknowledge TU Wien Bibliothek for financial support through its Open Access Funding Programme.

Appendix. Micromechanical quantification of the stresses in ITZs

The numerically quantified macroscopic stress $\boldsymbol{\Sigma}_{con}$ and the temperature field T_{con} are used for quantification of the macroscopic eigenstrains and strains, $\boldsymbol{E}^{e}_{con}$ and $\boldsymbol{E}_{con}$, respectively, given as

$$\boldsymbol{E}^{e}_{con} = \alpha_{con}\,\Delta T\,\mathbf{1}, \tag{38}$$

and

$$\boldsymbol{E}_{con} = \mathbb{C}^{-1}_{con} : \boldsymbol{\Sigma}_{con} + \boldsymbol{E}^{e}_{con}, \tag{39}$$

where $\mathbb{C}^{-1}_{con}$ represents the inverse of the elasticity tensor of the homogenized concrete, quantified as

$$\mathbb{C}_{con} = 3k_{con}\mathbb{I}_{vol} + 2\mu_{con}\mathbb{I}_{dev}, \tag{40}$$

with the bulk and shear modulus of concrete, k_{con} and μ_{con}, respectively, previously quantified from Eqs. (28) and (29). $\mathbb{I}_{vol}$ and $\mathbb{I}_{dev}$ represent the volumetric and deviatoric part of the symmetric fourth-order unit tensor. The volume-average of the microscopic strains of mortar and coarse aggregates are obtained as

$$\boldsymbol{\varepsilon}_{p} = \mathbb{A}_{p} : \boldsymbol{E}_{con} + \sum_{q=mort,cagg} \mathbb{D}_{pq} : \boldsymbol{\varepsilon}^{e}_{q} \quad , \quad p = mort, cagg, \tag{41}$$

where $\mathbb{A}_{p}$ and $\mathbb{D}_{pq}$ stand for the strain concentration tensor and the eigenstrain influence tensor, see [4,79] for details. Following the linear law of elasticity, the volume-average of the microscopic stresses can be determined as

$$\boldsymbol{\sigma}_{p} = \mathbb{C}_{p} : \left(\boldsymbol{\varepsilon}_{p} - \boldsymbol{\varepsilon}^{e}_{p}\right) \quad , \quad p = mort, cagg \tag{42}$$

The microscopic stress and strain tensors of the coarse aggregates are transformed from the Cartesian coordinate system into the local spherical coordinate system, as shown in Fig. 12, by means of the transformation matrix

$$\boldsymbol{Q} = \begin{bmatrix} \cos\zeta\sin\theta & \sin\zeta\sin\theta & \cos\theta \\ \cos\zeta\cos\theta & \sin\zeta\cos\theta & -\sin\theta \\ -\sin\zeta & \cos\zeta & 0 \end{bmatrix}. \tag{43}$$

The transformations from Cartesian coordinates to spherical coordinates follow as

$$\boldsymbol{\sigma}_{cagg}(r,\theta,\zeta) = \boldsymbol{Q}\cdot\boldsymbol{\sigma}_{cagg}(x,y,z)\cdot\boldsymbol{Q}^{T}, \tag{44}$$

$$\boldsymbol{\varepsilon}_{cagg}(r,\theta,\zeta) = \boldsymbol{Q}\cdot\boldsymbol{\varepsilon}_{cagg}(x,y,z)\cdot\boldsymbol{Q}^{T}, \tag{45}$$

with $\boldsymbol{Q}^{T}$ as the transpose of $\boldsymbol{Q}$.

Considering the continuity of the traction vectors and displacement vectors across the two-dimensional interface ($r = r_{cagg}$) between the coarse aggregates and the ITZ, gives access to the three stress and strain components of the ITZ as

$$\begin{cases} \sigma_{ITZ,rr}(\theta,\zeta) = \sigma_{cagg,rr}(\theta,\zeta) \\ \sigma_{ITZ,r\theta}(\theta,\zeta) = \sigma_{cagg,r\theta}(\theta,\zeta) \\ \sigma_{ITZ,r\zeta}(\theta,\zeta) = \sigma_{cagg,r\zeta}(\theta,\zeta) \end{cases} \tag{46}$$

and

$$\begin{cases} \varepsilon_{ITZ,\theta\theta}(\theta,\zeta) = \varepsilon_{cagg,\theta\theta}(\theta,\zeta) \\ \varepsilon_{ITZ,\zeta\zeta}(\theta,\zeta) = \varepsilon_{cagg,\zeta\zeta}(\theta,\zeta) \\ \varepsilon_{ITZ,\theta\zeta}(\theta,\zeta) = \varepsilon_{cagg,\theta\zeta}(\theta,\zeta) \end{cases}. \tag{47}$$

The other three stress and strain components can be determined by making use of the thermoelasticity law of the ITZ:

$$\begin{cases} \sigma_{ITZ,\theta\theta}(\theta,\zeta) = \left[4\mu_{ITZ}(3k_{ITZ}+\mu_{ITZ})\varepsilon_{ITZ,\theta\theta} + (3k_{ITZ}-2\mu_{ITZ})\left(2\mu_{ITZ}\varepsilon_{ITZ,\zeta\zeta}+\sigma_{ITZ,rr}\right) \right. \\ \qquad \left. - 18k_{ITZ}\mu_{ITZ}\alpha_{ITZ}\Delta T\right]/(3k_{ITZ}+4\mu_{ITZ}) \\ \sigma_{ITZ,\zeta\zeta}(\theta,\zeta) = \left[4\mu_{ITZ}(3k_{ITZ}+\mu_{ITZ})\varepsilon_{ITZ,\zeta\zeta} + (3k_{ITZ}-2\mu_{ITZ})\left(2\mu_{ITZ}\varepsilon_{ITZ,\theta\theta}+\sigma_{ITZ,rr}\right) \right. \\ \qquad \left. - 18k_{ITZ}\mu_{ITZ}\alpha_{ITZ}\Delta T\right]/(3k_{ITZ}+4\mu_{ITZ}) \\ \sigma_{ITZ,\zeta\zeta}(\theta,\zeta) = 2\mu_{ITZ}\varepsilon_{ITZ,\theta\zeta} \end{cases} \tag{48}$$

and

$$\begin{cases} \varepsilon_{ITZ,rr}(\theta,\zeta) = \dfrac{3\sigma_{ITZ,rr} - (3k_{ITZ}-2\mu_{ITZ})\left(\varepsilon_{ITZ,\theta\theta}+\varepsilon_{ITZ,\zeta\zeta}\right) + 9k_{ITZ}\mu_{ITZ}\alpha_{ITZ}\Delta T}{(3k_{ITZ}+4\mu_{ITZ})} \\ \varepsilon_{ITZ,r\theta}(\theta,\zeta) = \dfrac{\sigma_{ITZ,r\theta}}{2\mu_{ITZ}} \\ \varepsilon_{ITZ,r\zeta}(\theta,\zeta) = \dfrac{\sigma_{ITZ,r\zeta}}{2\mu_{ITZ}} \end{cases}, \tag{49}$$

see [4] for details.

Data availability

Data will be made available on request.

References

[1] Jeong J, Zollinger DG. Environmental effects on the behavior of jointed plain concrete pavements. J Transp Eng 2005;131(2):140–8.
[2] Xiang Y, Zhao H, Liu J, Yang G, Hu Z, Chen J. Damage and fracture in in-service concrete structures subjected to large diurnal temperature variations based on phase-field approach. Structures 2024;65:106600.
[3] Saad S, Bashir R, Pantazopoulou S. Bridge decks under cold waves: implications of concrete's temperature-dependent CTE. Eng Struct 2024;314:118351.
[4] Wang H, Höller R, Aminbaghai M, Hellmich C, Yuan Y, Mang HA, Pichler BL. Concrete pavements subjected to hail showers: a semi-analytical thermoelastic multiscale analysis. Eng Struct 2019;200:109677.
[5] Belshe M, Mamlouk MS, Kaloush KE, Rodezno M. Temperature gradient and curling stresses in concrete pavement with and without open-graded friction course. J Transp Eng 2011;137(10):723–9.
[6] Grasley ZC. Internal relative humidity, drying stress gradients, and hygrothermal dilation of concrete (thesis). University of Illinois at Urbana-Champaign; 2003.
[7] Louhghalam A, Ulm F-J. Risk of pavement fracture due to eigenstresses at early ages and beyond. J Eng Mech 2016;142(12):04016105.
[8] Chen D, Zou J, Zhao L, Xu S, Xiang T, Liu C. Degradation of dynamic elastic modulus of concrete under periodic temperature-humidity action. Materials 2020;13(3):611.
[9] Huang H, An M, Wang Y, Yu Z, Ji W. Effect of environmental thermal fatigue on concrete performance based on mesostructural and microstructural analyses. Constr Build Mater 2019;207:450–62.
[10] Xia Y, Hao H, Zanardo G, Deeks A. Long term vibration monitoring of an RC slab: temperature and humidity effect. Eng Struct 2006;28(3):441–52.
[11] ACI Committee 201. Report 201.2 R-16 – guide to durable concrete (Tech. rep.). American Concrete Institute; 2016.
[12] Zhang K, Lei J, Wang Z, Yuan Q. A numerical algorithm for damage progression of reinforced concrete bridge piers during air temperature and solar radiation cycles. Eng Struct 2024;319:118876.
[13] Alungbe GD, Tia M, Bloomquist DG. Effects of aggregate, water/cement ratio, and curing on the coefficient of linear thermal expansion of concrete. Transp Res Rec 1992;1335:44–51.
[14] Emanuel JH, Hulsey JL. Prediction of the thermal coefficient of expansion of concrete. J Am Concr Inst 1977;74(4):149–55.
[15] Wang H, Mang H, Yuan Y, Pichler BL. Multiscale thermoelastic analysis of the thermal expansion coefficient and of microscopic thermal stresses of mature concrete. Materials 2019;12(17):2689.
[16] Mindess S, Young JF, Darwin D. Concrete. Englewood Cliffs: Prentice-Hall; 1981.
[17] Zhou M, Wu Z, Ouyang X, Hu X, Shi C. Mixture design methods for ultra-high-performance concrete - a review. Cem Concr Compos 2021;124:104242.
[18] Bonnell DGR, Harper FC. The thermal expansion of concrete. Engineering research. J Inst Civ Eng 1950;33(4):320–30.
[19] Naik TR, Kraus RN, Kumar R. Influence of types of coarse aggregates on the coefficient of thermal expansion of concrete. J Mater Civ Eng 2011;23(4):467–72.
[20] Chung Y, Shin H. Characterization of the coefficient of thermal expansion and its effect on the performance of portland cement concrete pavements. Can J Civ Eng 2011;38(2):175–83.
[21] Wang H, Hellmich C, Yuan Y, Mang H, Pichler B. May reversible water uptake/release by hydrates explain the thermal expansion of cement paste? - arguments from an inverse multiscale analysis. Cem Concr Res 2018;113:13–26.
[22] Grasley ZC, Lange DA, D'Ambrosia MD, Villalobos-Chapa S. Relative humidity in concrete. Concr Int 2006;28(10):51–7.
[23] Wyrzykowski M, McDonald PJ, Scrivener KL, Lura P. Water redistribution within the microstructure of cementitious materials due to temperature changes studied with ^{1}H NMR. J Phys Chem C 2017;121(50):27950–62.
[24] Asadi I, Shafigh P, Hassan ZFBA, Mahyuddin NB. Thermal conductivity of concrete - a review. J Build Eng 2018;20:81–93.
[25] Gomes MG, FloresColen I, Manga L, Soares A, De Brito J. The influence of moisture content on the thermal conductivity of external thermal mortars. Constr Build Mater 2017;135:279–86.
[26] Torelli G, Gillie M, Mandal P, Draup J, Tran V-X. A moisture-dependent thermomechanical constitutive model for concrete subjected to transient high temperatures. Eng Struct 2020;210:110170.
[27] Zhang J, Binder E, Wang H, Aminbaghai M, L.A. Pichler B, Yuan Y, Mang HA. On the added value of multi-scale modeling of concrete. Front Struct Civ Eng 2022;16(1):1–23.
[28] Fu Y, Wong Y, Tang C, Poon CS. Thermal induced stress and associated cracking in cement-based composite at elevated temperatures - part I: thermal cracking around single inclusion. Cem Concr Compos 2004;26(2):99–111.
[29] Fu Y, Wong Y, Poon C, Tang C, Lin P. Experimental study of micro/macro crack development and stress-strain relations of cement-based composite materials at elevated temperatures. Cem Concr Res 2004;34(5):789–97.
[30] Willam K, Rhee I, Shing B. Interface damage model for thermomechanical degradation of heterogeneous materials. Comput Methods Appl Mech Eng 2004;193(30-32):3327–50.
[31] Wu T, Wriggers P. Multiscale diffusion–thermal–mechanical cohesive zone model for concrete. Comput Mech 2015;55:999–1016.
[32] Chen W, Gu X, Zhang Q, Xia X. A refined thermo-mechanical fully coupled peridynamics with application to concrete cracking. Eng Fract Mech 2021;242:107463.
[33] Li X, Gu X, Xia X, Madenci E, Chen A, Zhang Q. Peridynamic simulation of micro-internal damage and macro-mechanical properties of cement paste under freeze-thaw cycles. J Build Eng 2024;93:109759.
[34] Pal B, Ramaswamy A. A meso-scale study to predict high-temperature behavior of concrete structures in a hygral-thermal-chemical-mechanical framework. Constr Build Mater 2024;421:135671.
[35] de Borst R, Remmers JJ, Needleman A. Mesh-independent discrete numerical representations of cohesive-zone models. Eng Fract Mech 2006;73(2):160–77.
[36] Turon A, Davila CG, Camanho PP, Costa J. An engineering solution for mesh size effects in the simulation of delamination using cohesive zone models. Eng Fract Mech 2007;74(10):1665–82.
[37] Miao K, Pan Z, Fang X, Chen A. Fire-induced damage behaviour in corrosion-damaged concrete: Thermal-mechanical coupling phase field meso-scale modeling. J Mech Phys Solids 2025;196:106041.
[38] Peng Z, Wang Q, Zhou W, Chang X, Yue Q, Huang C. Meso-scale simulation of thermal fracture in concrete based on the coupled thermal–mechanical phase-field model. Constr Build Mater 2023;403:133095.

[39] Prakash PR, Pulatsu B, Lourenço PB, Azenha M, Pereira JM. A meso-scale discrete element method framework to simulate thermo-mechanical failure of concrete subjected to elevated temperatures. Eng Fract Mech 2020;239:107269.
[40] Sinaie S, Heidarpour A, Zhao X. A micro-mechanical parametric study on the strength degradation of concrete due to temperature exposure using the discrete element method. Int J Solids Struct 2016;88:165–77.
[41] Pham DT, Nguyen TD, Vu MN, Chinkulkijniwat A. Mesoscale approach to numerical modelling of thermo-mechanical behaviour of concrete at high temperature. Eur J Environ Civ Eng 2021;25(7):1329–48.
[42] Borden MJ, Verhoosel CV, Scott MA, Hughes TJ, Landis CM. A phase-field description of dynamic brittle fracture. Comput Methods Appl Mech Eng 2012;217:77–95.
[43] Miehe C, Hofacker M, Welschinger F. A phase field model for rate-independent crack propagation: robust algorithmic implementation based on operator splits. Comput Methods Appl Mech Eng 2010;199(45-48):2765–78.
[44] Miehe C, Welschinger F, Hofacker M. Thermodynamically consistent phase-field models of fracture: variational principles and multi-field FE implementations. Int J Numer Methods Eng 2010;83(10):1273–311.
[45] Ambati M, Gerasimov T, De Lorenzis L. A review on phase-field models of brittle fracture and a new fast hybrid formulation. Comput Mech 2015;55:383–405.
[46] Chen L, Zhao Y. From classical thermodynamics to phase-field method. Prog Mater Sci 2022;124:100868.
[47] Schreiber C, Müller R, Kuhn C. Phase field simulation of fatigue crack propagation under complex load situations. Arch Appl Mech 2021;91(2):563–77.
[48] Seleš K, Aldakheel F, Tonković Z, Sorić J, Wriggers P. A general phase-field model for fatigue failure in brittle and ductile solids. Comput Mech 2021;67:1431–52.
[49] Liu S, Wang Z, Zhang Y, Kou M, Bi J. The phase-field simulations of blasting failure in granites. Int J Impact Eng 2022;167:104274.
[50] Zhang P, Hu X, Yang S, Yao W. Modelling progressive failure in multi-phase materials using a phase field method. Eng Fract Mech 2019;209:105–24.
[51] Zhang P, Dai J, Das CS, Zheng J. A fully coupled meso-scale electro-chemo-mechanical phase field method for corrosion-induced fracture in concrete. Int J Solids Struct 2023;267:112165.
[52] Zhang P, Dai J. New mesoscale phase field model for analysis of FRP-to-concrete bonded joints. J Compos Constr 2024;28(3):04024007.
[53] Miehe C, Schaenzel L, Ulmer H. Phase field modeling of fracture in multi-physics problems. Part I. Balance of crack surface and failure criteria for brittle crack propagation in thermo-elastic solids. Comput Methods Appl Mech Eng 2015;294:449–85.
[54] Miao X, Kolditz O, Nagel T. Modelling thermal performance degradation of high and low-temperature solid thermal energy storage due to cracking processes using a phase-field approach. Energy Convers Manag 2019;180:977–89.
[55] Scrivener KL, Crumbie AK, Laugesen P. The interfacial transition zone (ITZ) between cement paste and aggregate in concrete. Interface Sci 2004;12:411–21.
[56] Schlangen E, Van Mier J. Simple lattice model for numerical simulation of fracture of concrete materials and structures. Mater Struct 1992;25:534–42.
[57] Walraven JC. Aggregate interlock: a theoretical and experimental analysis (thesis). Delft University; 1980.
[58] Qin Y, Hiller JE. Simulating moisture distribution within concrete pavement slabs: model development and sensitivity study. Mater Struct 2014;47:351–65.
[59] Schmid SJ, Díaz Flores R, Aminbaghai M, Eberhardsteiner L, Wang H, Blab R, Pichler BL. Significance of eigenstresses and curling stresses for total thermal stresses in a concrete slab, as a function of subgrade stiffness. Int J Pavement Eng 2023;24(2):2091136.
[60] Murthy V. Textbook of soil mechanics and foundation engineering. New Delhi: CBS Publishers & Distributors/Alkem Company (S); 2007.
[61] Wang H, Yuan Y, Mang HA, Ai Q, Huang X, Pichler BL. Thermal stresses in rectangular concrete beams, resulting from constraints at microstructure, cross-section, and supports. Eur J MechA/Solids 2022;93:104495.
[62] Nilsen AU, Monteiro PJ. Concrete: a three phase material. Cem Concr Res 1993;23(1):147–51.
[63] Simeonov P, Ahmad S. Effect of transition zone on the elastic behavior of cement-based composites. Cem Concr Res 1995;25(1):165–76.
[64] Haecker C-J, Garboczi EJ, Bullard JW, Bohn R, Sun Z, Shah SP, Voigt T. Modeling the linear elastic properties of portland cement paste. Cem Concr Res 2005;35(10):1948–60.
[65] Gudmundsson A. Rock fractures in geological processes. Cambridge, UK: Cambridge University Press; 2011.
[66] Wang F, Shao J, Huang H. A phase-field modeling method for the mixed-mode fracture of brittle materials based on spectral decomposition. Eng Fract Mech 2021;242:107473.
[67] Hu X, Xu H, Xi X, Zhang P, Yang S. Meso-scale phase field modelling of reinforced concrete structures subjected to corrosion of multiple reinforcements. Constr Build Mater 2022;321:126376.
[68] Meyers S. Thermal expansion characteristics of hardened cement paste and of concrete. Highway Research Board Proceedings, 30; 1951. p. 193–203.
[69] Mitchell LJ. Thermal expansion tests on aggregates, neat cements, and concretes. Proceedings of the American Society for Testing and Materials, 53; 1953. p. 963–77.
[70] Dettling H., 1962. Die Wärmedehnung des Zementsteines, der Gesteine und der Betone [Thermal expansion of the cement paste, the aggregates, and concretes] (thesis). Technische Hochschule Stuttgart.
[71] Meng Z, Liu Q-F, She W, Cai Y, Yang J, Iqbal MF. Electrochemical deposition method for load-induced crack repair of reinforced concrete structures: a numerical study. Eng Struct 2021;246:112903.
[72] Skarżyński Ł, Marzec I. Shear fracture of longitudinally reinforced concrete beams under bending using digital image correlation and FE simulations with concrete micro-structure based on X-ray micro-computed tomography images. Constr Build Mater 2021;274:122116.
[73] Shi X, Fwa T, Tan S. Warping stresses in concrete pavements on pasternak foundation. J Transp Eng 1993;119(6):905–13.
[74] Fwa T, Shi X, Tan S. Use of pasternak foundation model in concrete pavement analysis. J Transp Eng 1996;122(4):323–8.
[75] Zokaei-Ashtiani A, Carrasco C, Nazarian S. Effect of nonlinear temperature gradient on responses of jointed concrete pavements. Proceedings of the International Conferences on the Bearing Capacity of Roads, Railways and Airfields. 2013. p. 423–33.
[76] Singh K, Ghosh G. Stress behavior of concrete pavement. Mater Today Proc 2022;55:246–9.
[77] Zokaei-Ashtiani A, Carrasco C, Nazarian S. Finite element modeling of slab-foundation interaction on rigid pavement applications. Comput Geotech 2014;62:118–27.
[78] Zhang H, Qiu Y. Model for calculation of thermal stresses in concrete pavement slabs with refined non-linear deformation constraints. Road Mater Pav Des 2024;25(4):820–37.
[79] Ghabezloo S. Micromechanics analysis of thermal expansion and thermal pressurization of a hardened cement paste. Cem Concr Res 2011;41(5):520–32.